Optimal Energy Management of a Residential-based Hybrid Renewable Energy System Using Rule-based Real-time control and 2D Dynamic Programming Optimization Method

Mohammad Jafari*, Zahra Malekjamshidi

School of Electrical and Data Engineering, Faculty of Engineering and IT, University of Technology Sydney, 15 Broadway, NSW 2007, Australia

*Corresponding author
E-mail address: mohammad.jafari@uts.edu.au

ARTICLE INFO

Article history:
Received 23 June 18
Received in revised form 08 May 19

Keywords:
Energy management
Real-time
Renewable energy system
Residential
Rule-based

ABSTRACT

This paper presents a magnetically coupled hybrid renewable energy system (RES) for residential applications. The proposed system integrates the energies of a set of PV panels, a fuel cell stack, and a battery using a multi-winding magnetic link to supply a residential load. It can operate in multiple grid-connected and off-grid operation modes. An energy management unit including an off-line dynamic programming-based optimization stage and a real-time rule-based controller is designed to optimally control the power flow in the system according to the provided energy plan. The system is designed according to the required standards of the grid-connected residential RES. Different sections of the proposed system including steady-state operation, control techniques, energy management method and hardware design are studied in brief. A prototype of the proposed system is developed and experimentally tested for an energy management scenario considering both sunny and cloudy profiles of the PV generation. The energy distribution and cost analysis approved the benefits of the proposed system for residential consumers.

1. Introduction

Although various distributed generation (DG) systems based on renewable energy sources, such as solar and wind have been used for many years, it is still a serious challenge to integrate them into the conventional distribution networks since these renewable energy sources are intermittent, resulting in poor power quality. This problem can be effectively solved by adopting the concept of smart micro-grids, which integrate the renewable power generation, energy storage, and consumption closely through intelligent communication and control strategies [1]. To implement this, power electronic converters capable of bidirectional power flow and four-quadrant operation are required [2]. Special control strategies, embedded in the power converter controllers and micro-grid control center, should be developed to control the power quality and maintain steady voltage and frequency in the islanded and grid-connected modes [2]-[3]. Residential consumers as an important portion of electricity consumers are changing from passive energy users to active small-scale energy producers. The rooftop solar systems have been growing continuously in Australia over the past decade and increased to about 1.6 million in 2017 [4]. The annual number of solar PV systems installed in the residential and commercial sectors decreased slightly after a sharp increase over the past decade although, the average size of the PV systems has been increasing from 1 kW to about 5.5 kW as illustrated in Fig.1 [5]. Despite their advantages, the intermittency nature of most of the renewable resources still is a challenge which can be resolved by hybridization. A hybrid renewable energy system (HRES) combines the energies of several renewable sources to supply the load [6]. It may need an energy storage device such as a battery to save the energy for the times that none of the sources is available [7].

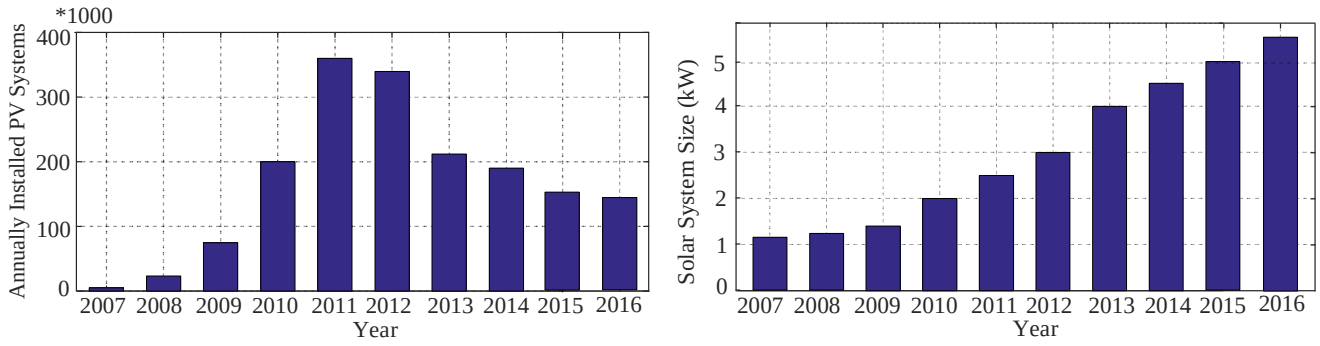

(a) (b)

Fig.1- (a) Number of solar PV systems installed annually, and (b) size of the installed solar systems in Australia over the past decade [5].

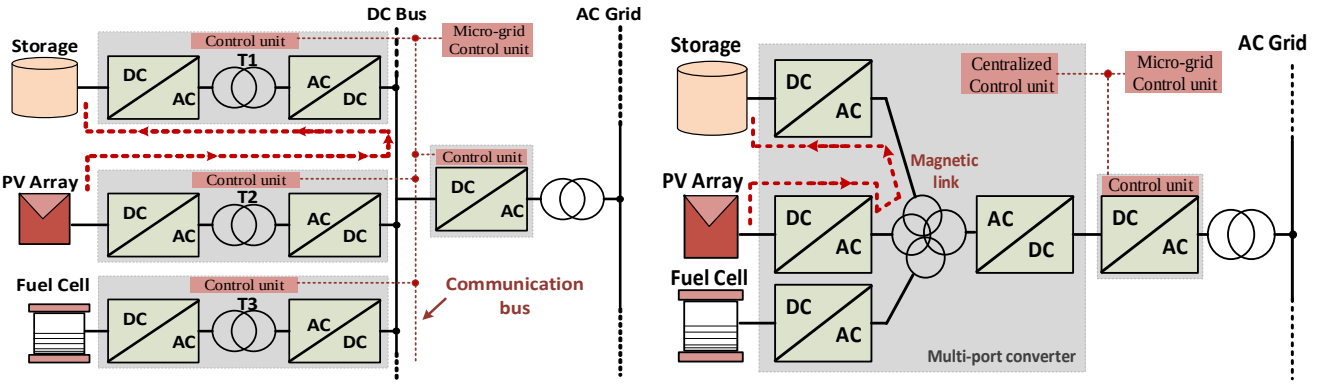

(a) (b)

Fig.2- Structure of a hybrid renewable energy system, (a) without the magnetic link, and (b) with the magnetic link

The storage device also can be used to smooth the transition from one source to another and balance the energy transfer in the case of using sources with a low dynamic response such as fuel cells [8]. A widely used hybrid system includes wind and solar energy sources providing a more reliable source due to their complementary nature. To integrate the outputs of renewable energy sources to supply the load, different HRES topologies are proposed in the literature.

The most common structures include several voltage conversion blocks to adapt the output voltage of each source, storage or load to the common intermediate electrical ac or dc bus [9]. Fig.2 (a) shows an example of a residential HRES including multiple voltage conversion blocks and a common electrical dc bus. The main drawback of such a topology is its control complexity even if each converter has a simple structure and control method. A multi-port converter topology as a single power processing unit is an alternative for the multi-conversion based systems. This can effectively reduce the total size and cost of the HRES, and individual controllers can be compacted into a centralized control unit [10]. On the other hand, common problems of electrical buses like voltage and frequency instabilities are avoided. Due to this many attempts have been made to explore new topologies of multi-port converters for HRESs [8]-[11]. The proposed topologies operate mainly based on the series or parallel connection of voltage or current source cells [12], time sharing [13] and magnetic coupling [14] concepts. Nevertheless, a few of these topologies can be modified for the household application according to the required standards [15]-[17]. Considering safety requirements and range of processing power, magnetically coupled multi-port converters are a proper candidate for residential applications [14]. A topology of a magnetically coupled HRES is proposed in Fig.2 (b). Comparing this structure with the one presented in Fig.2 (a) shows that the magnetic link shortens the power flow path and reduces the number of converters which increases the system efficiency and reduces the size and cost. Despite the remarked advantages, design and development of the multi-winding magnetic links with a large number of windings is complex [9], [14]. Therefore, a more efficient and simpler topology is suggested in this paper, by using a combination of electrical dc bus and the magnetic link. Besides the system's topology and configuration, different household energy management techniques are employed to save the household energy bills with less influence on convenience and healthiness of the occupants [18]-[25]. The reported techniques are mainly related to the demand–side management [18], [19], off-line optimization methods [20], [21] and real-time rule-based power flow control techniques [22], [23]. Other management techniques using fuzzy logic and artificial neural networks also have been reported [24]-[26].

Dynamic programming as an attractive optimization technique has been used as an optimization technique in several energy management systems including PV/battery HRESs [20] and electric vehicles [27]. It doesn't need any particular mathematical solver and is independent of the nature of the system constraints (linear or nonlinear, convex or concave, etc.) [20].

In this paper, an HRES topology is proposed for residential application. The system integrates the output energy of a PV, fuel cell and battery to supply the loads. The proposed system can operate in a large number of grid-connected and off-grid operation modes (totally 18 modes) compared to the previously reported systems. Furthermore, it considers more effective elements such as battery charge and discharge characteristics and efficiency performance of the converter in the optimization process. The paper is continuing the work presented by authors in [28]. However, more attention is paid to the energy management system and the hardware features which adapt the system to the recent standards of grid-connected HRESs. Therefore, a brief review

on the main mandatory standards of the grid-connected residential renewable energy systems in terms of harmonic contents, voltage and frequency variation range has been presented in this paper.

As the main contribution, detail of a novel energy management technique comprising an off-line 2D dynamic programming-based optimization stage and a real-time rule-based controller is presented. Therefore, both the real-time value of the system parameters and the long-term predictions of the energy generation and consumption, and the energy cost profile have been taken into account. Furthermore, the efficiency performances of the converters and the transformer are included in the optimization process. Some control techniques and hardware designs that are employed to adapt the system to the current standards of the grid-connected HRESs [15]-[17]. A synchronized bus voltage stabilization (SBVS) technique is designed in the converter control loop to improve the soft switching range and efficiency of the TAB converter. The low-frequency ripples propagated from inverter on the fuel cell and the PV dc buses is limited by using a compensation block in the inverter current control loop. The system is protected by designing appropriate voltage and frequency fault detection circuits according to the required standards [15]-[17].

The rest of the paper is organized as follows. The steady-state operation and control technique of the proposed system are discussed in section 2 and the operation modes and energy management method in section 3. Section 4 reviews the hardware design and development. The experimental test results are presented in section 5 and conclusions in section 6.

2. Operation and control in steady state

The topology of the proposed HRES and the control systems are illustrated in Fig.3. As can be seen, the system contains a PV array and a fuel cell stack as renewable energy sources and a battery bank as energy storage to supply a 4.5 kW residential load. The proposed topology includes three H-bridge dc-ac converters in port one, two and three which forms a triple active bridge (TAB) dc-dc converter. Port four, includes a bidirectional buck-boost converter to link the battery to dc bus and the PV is linked to the dc bus through an interleaved boost converter. The TAB converter also can operate in dual active bridge (DAB) mode when only two bridges are active. The proposed topology and the control techniques can be generally used for a hybrid renewable energy system with any type of input source. However, a special consideration regarding characteristics of each energy source should be taken into account.

In port three, the switching devices S31-S34 have been shared between the H-bridge dc-ac converter and the interleaved boost converter. The interleaved topology reduces the high-frequency current ripple of the PV port which improves the MPPT performance and the efficiency [29]. It also boosts the PV output voltage and transfers the extracted power to the dc bus capacitor C_3. To perform the maximum power point tracking (MPPT), the PV output voltage and current are sent to the energy management unit (EMU) and are used to define the appropriate reference voltage (V^*_{PV}) for PV output according to an incremental conductance MPPT method [30]. A double-loop control system including an inner inductor current control and outer PV voltage control is used to maintain the MPPT by changing the duty cycle d_1.

On the other hand, the phase shift angle φ_{31} is used to regulate the dc bus voltage, V_{b3} on the reference value (V^*_{b3}). The reference voltage is defined as a function of dc bus voltage of port one (V_{b1}), to synchronize the voltage variations of ports three and one. To realize the SBVS technique, the volt-second product of the voltage waveforms on all the three windings of the magnetic link should be kept equal [8]. Therefore, current in the windings of the magnetic link and consequently the conduction loss is minimized, and the soft switching operation is achieved for the entire operating range of the TAB converter [8], [9]. As a common problem, a low-frequency ripple (f=2ω) is reflected from the inverter output on the high-voltage dc bus. The resultant ripple also is transferred to the low-voltage dc-bus which can deteriorate the MPPT performance. To reduce the effect, a proportional-integral-resonant (PIR) controller is implemented by adding a resonance element to the PI controller transfer function in the inner current control loop and presented as:

$$C_{i-PV}(s) = \overbrace{k_P + \frac{k_I}{S}}^{PI} + \overbrace{\frac{2\omega S}{S^2 + 4\pi S + (2\omega)^2}}^{resonant\ \ element} \tag{1}$$

where k_P and k_I are known as the proportional and integral coefficients respectively, and ω=100π for f=50 Hz. The fuel cell stack in the port two is mainly used as a backup energy source and is directly connected to the H-bridge conversion cell in the TAB converter. The power flow between ports two and one (P_2) is controlled by the phase shift angle φ_{21} according to the reference signal (P_2^*) generated by the EMU as presented in Fig.3. The power flow in reverse direction from the grid to the battery is achieved by reversing P_2 and P_2^* signals and activating battery port in buck operation mode. The battery as the main energy storage device is linked to dc bus by using a bidirectional buck-boost converter. It also is used in standby mode to stabilize the voltage of the dc bus due to the slow dynamic response of the fuel cell. In the first case, the reference voltage (V^*_{b2}) is determined equal to the nominal bus voltage and in the second case is defined as $V^*_{b2}=(N_2/N_1)V_{b1}$ according to the SBVS technique using dc bus voltage in port one (V_{b1}) as a reference. The converter is always operating in continuous conduction mode (CCM), and the charging mode (buck) or discharging mode (boost) operation is defined by the duty ratio of the gate drive signal applied to S_2 presented as d_4, compared to a critical duty ratio d_4^* and briefly can be presented as: $d > d_4^* \rightarrow$Boost, $d < d_4^* \rightarrow$Buck. The critical duty ratio d_4^* where the average of the battery current is equal to zero is determined by $d_4^* = 1 - V_{bat}/V_{b2}$ where V_{bat} and V_{b2} represent the battery and the dc bus voltages respectively [31].

The H-bridge converter in Port one transfers the output power from PV, fuel cell or stored power in the battery to the high-voltage dc bus and further to the grid-connected inverter by using leading phase shift angles φ_{21} and φ_{31} as illustrated in Fig.3. The single-phase bidirectional inverter then converts the high voltage dc bus to the low-frequency ac voltage supplied to the residential load and the grid. The converter can be used reversely as a rectifier to convert

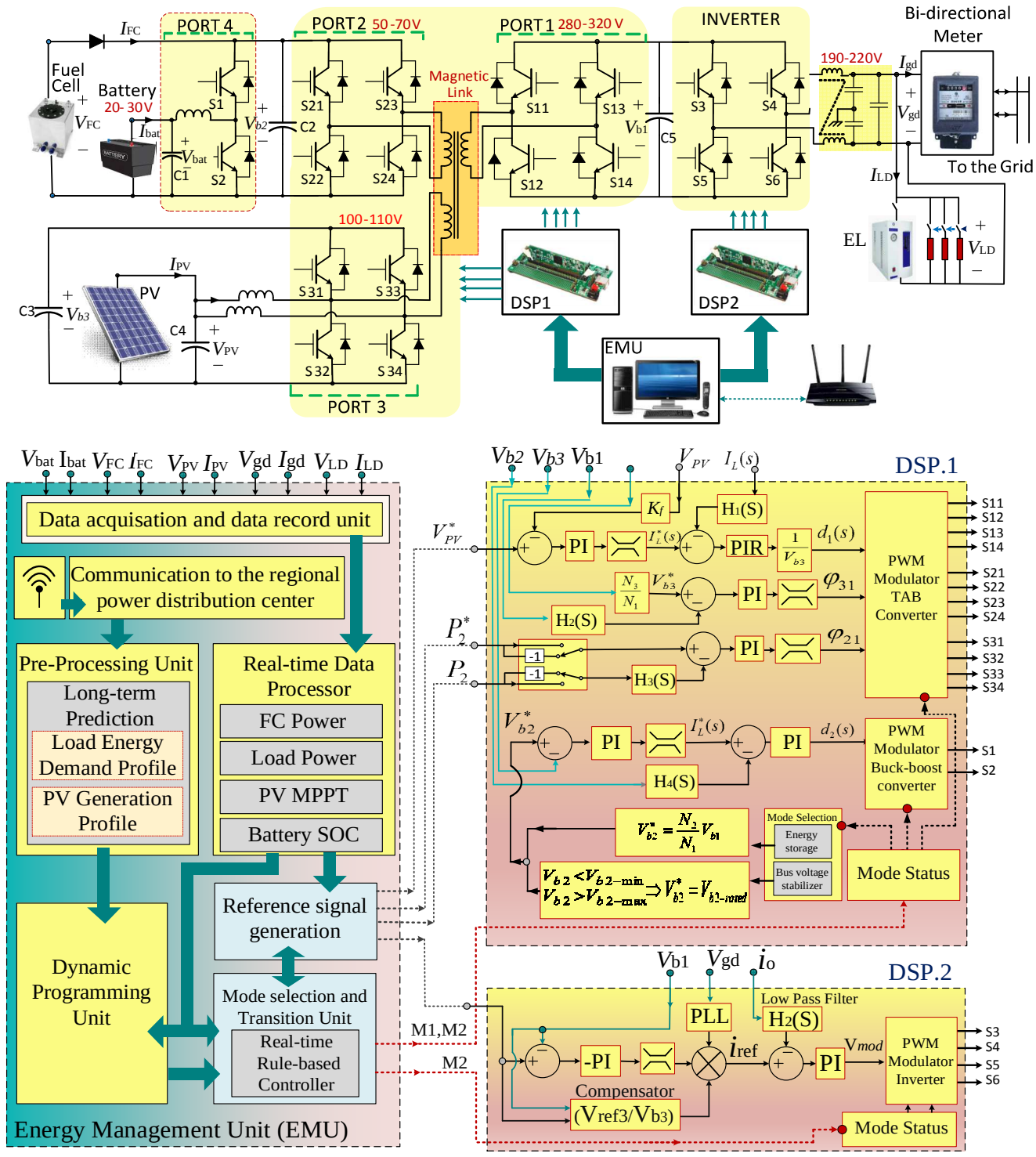

Fig.3- Structure of the proposed hybrid renewable energy system, control system and energy management unit

the ac voltage of the grid to the high-voltage dc and transfer the power from the utility grid to the battery. A second DSP controls the inverter due to the limited number of PWM output signals.

In the single-phase inverter a double loop control system is designed to control the output current directly to follow the utility grid voltage. A phase-locked loop (PLL) block is used to generate a sinusoidal reference signal synchronized with the grid in the grid-connected condition or independently in the islanding mode. This results in a unity power factor and relatively low THD according to the required standards and fast dynamic response [32], [33]. To control the direction of power flow, the reference signal for high voltage dc bus (V_{b1}^*) can be adjusted to less than the actual value (V_{b1}) for operating in

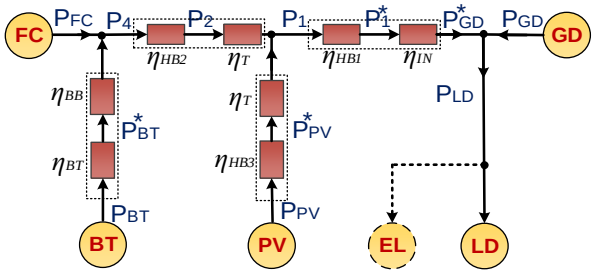

Fig.4- Simplified power flow model of the system [27]

inverter mode and more than the actual value for rectifier mode. In the inverter operation mode, a voltage ripple with the frequency $2f$ (f=50 Hz) is reflected from the inverter output on the high-voltage dc bus [29]. The reflected ripple is transferred on the dc buses of the PV port and the fuel cell ports which can deteriorate the MPPT performance. To reduce this effect, a feed-forward signal equal to (V_{b1}^*/V_{b1}) is applied to the inverter current control loop as presented in Fig. 3. This applies a signal with reverse variation and the frequency $2f$ to the output filter inductor current which reduces the low-frequency ripple reflected on the high-voltage dc bus. The practical effect of using this block on the propagated low-frequency ripple will be presented in the experimental results. An electrolyzer is considered as a part of the residential load to increase the energy management flexibility of the system and also generates the required Hydrogen for the fuel cell operation. The proportional and integral coefficients of the PI compensators in all controllers are determined according to the desirable crossing frequency and phase margins of the current and voltage control loops [34]. The transfer functions presented as *H(S)* are low-pass filters. Next section reviews the operation modes and the energy management technique in the proposed HRES.

3. Analysis of the energy management technique

The EMU defines the active operating mode of the system according to the control objectives, energy management scenario, energy cost and availability, and the load demand. As presented in Fig.3, the EMU includes a data acquisition and record unit to receive the voltage and current signals of the converter ports. The received data is later sent to a real-time data processor and are used to calculate the fuel cell and load powers, estimate the battery SOC and perform the MPPT process. On the other hand, the load demand and PV power generation profiles are estimated based on the historically recorded data and the information received from the regional power distribution control center in a pre-processing unit. The resultant values are used to generate the reference signals for local controllers and determine the operation mode. The operation modes are defined based on the power flow direction between the active components of the renewable energy system. The simplified power flow model of the system illustrated in Fig.4 is used to present the possible operation modes [28]. In this model, each of the dc-ac or dc-dc conversion cells and the transformer are presented as a simple power processing block. Fig.5 shows the possible grid-connected and off-grid operation modes of the system. The operation mode M1 where the load is supplied by the grid only in grid-connected or by the battery in off-grid conditions is defined as the basic mode. Therefore, it is a common status in all operation modes and is used as a bridging mode in most of the mode transitions process as is a common status between all operation modes.

In this paper, the optimal operation mode is determined using a two-scale control strategy. As presented in Fig.3, an off-line dynamic programming unit (DPU) is used to optimally determine the available capacity of the storage devices according to the long-term energy plans. The resultant variation ranges then are used in the real-time mode selection and transition unit (MSTU) to be used for defining the appropriate operation mode. A mode transition strategy is designed to avoid the instabilities during the change over from one operation mode to another. The transition between two operation modes can be performed directly or through a bridging mode depending on the origin and destination mode conditions. The MSTU operates based on a real-time rule-based controller to determine the next operation mode. It also contains a state transition diagram (STD) to determine the transition path between the operation modes as presented in Fig.6. Furthermore, the main steps of the transition process and the required conditions are controlled. This includes the evaluation of available stored and demanded energies of the components involved in the destination mode, controlling the transition steps and generation of reference and command signals for the device level controllers. The proposed system can be used as a platform for development and test of different energy management techniques as all required signals from PV, fuel cell, battery, residential load and the main grid are received by the EMU as presented in Fig.3. On the other hand, it is assumed that the micro-grid control center provides the grid energy cost for the next time interval. The forecasted profile of the load demand is obtained from historical data recorded in EMU. The predicted PV power generation profile is estimated using climatological data provided by the power distribution control center for the next time-frame and is regularly updated. Details of the controllers are discussed in the next sections.

3.1. Dynamic programming unit

The DP is an optimisation method which defines the best arrangement of operation modes to satisfy a predefined objective function during a moving timeframe [20]. The timeframe is divided into several time steps starting from the current time to a future and is updated at the beginning of each time step by moving one step ahead. The process includes sequential stages of applying a change (positive or negative) to the system variables for a time step and estimation of the system status at the end of the time step accordingly. The system constraints should be taken into account for each time step. The applied changes to the system variables lead to a particular variation path during the timeframe. The process is performed for all possible paths and the path with the best result according to the objective function is selected. Finally, the system variables and operation mode are changed according to the selected path. The method accepts any linear or non-linear, convex or concave constraints. However, selecting small time-steps with the large time-frames needs large

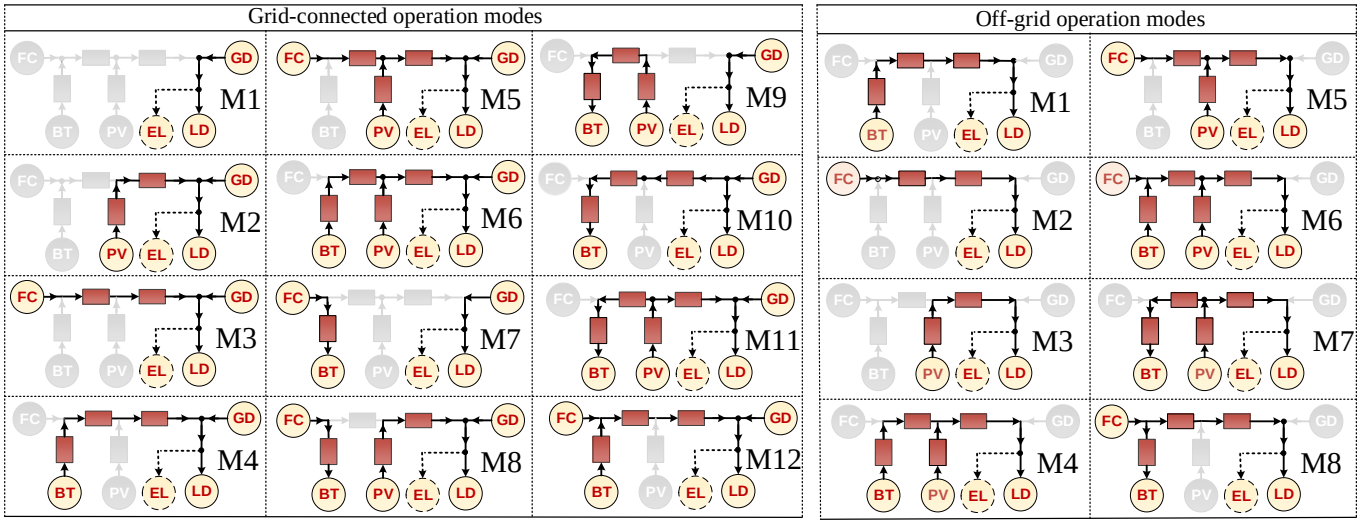

Fig.5-The grid-connected and off-grid operation modes of the proposed renewable energy system

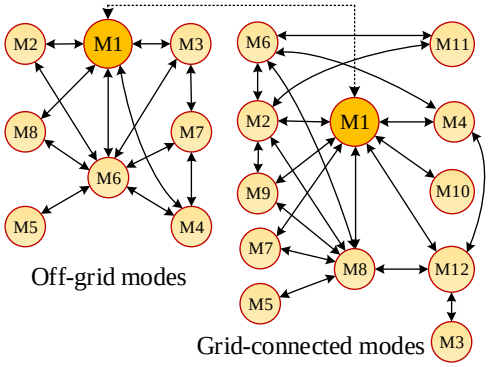

Fig.6-State transition diagram of the MTSU

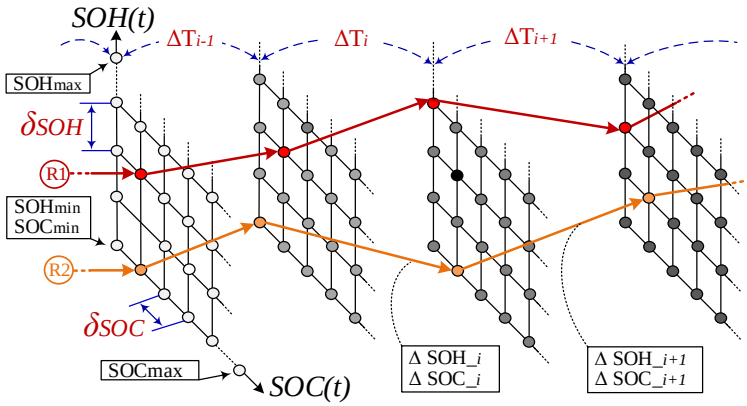

Fig.7-The Trajectory of 2D-dynamic programming

memory space and may result in the extensive computation time. On the other hand, the characteristics of the system components such as converter efficiency performance and the battery power loss during the charge and discharge processes can be taken into account in the optimization and mode selection process.

In this paper, the objective function of the EMU is to find a scheduled variation path for the battery state of charge (SOC) and the fuel cell state of hydrogen (SOH) which minimizes the energy cost of the system during the related time-frame. Fig.7 illustrates the trajectory of the proposed DP problem. The pre-processing unit provides the forecasted profiles of the load demand and PV generation (referring to Fig.3) and the energy tariff profile of the utility grid for the next timeframe is received regularly from the smart grid control centre at the beginning of each time step. The optimization problem starts with power balance equations of the system according to Fig.4 as

$$P_{FC}+P_{PV}+P_{BT}+P_{GD}-P_{LD}-P_{EL}-P_{LS}=0 \tag{2}$$

where P_{LS} is the total power loss in the system and can be decomposed into the transformer loss ($P_{LS,T}$) and the converters loss ($P_{LS,C}$) as

$$P_{LS} = P_{LS,T} + P_{LS,C} \tag{3}$$

The power loss is defined by the conduction and switching losses in the H-bridge units ($P_{LS,HB}$), buck-boost dc-dc converter ($P_{LS,BB}$) and the single-phase inverter ($P_{LS,IN}$) from

$$P_{LS,C} = (P_{LS,HB1} + P_{LS,HB2} + P_{LS,HB3}) + P_{LS,BBC} + P_{LS,IN} \tag{4}$$

For the sake of simplicity, the transformer conduction loss and the converter conduction loss are combined. The battery efficiency is also merged into the buck-boost converter efficiency. The power loss in each conversion unit is defined by using the converter efficiency characteristic graph as a function of the input power to the nominal power. The converter efficiency curve can be estimated based on the normalized input power using a fitted second or third-order polynomial as presented in Fig.8. The battery loss also can be found as a function of the battery charging or discharging power taking into

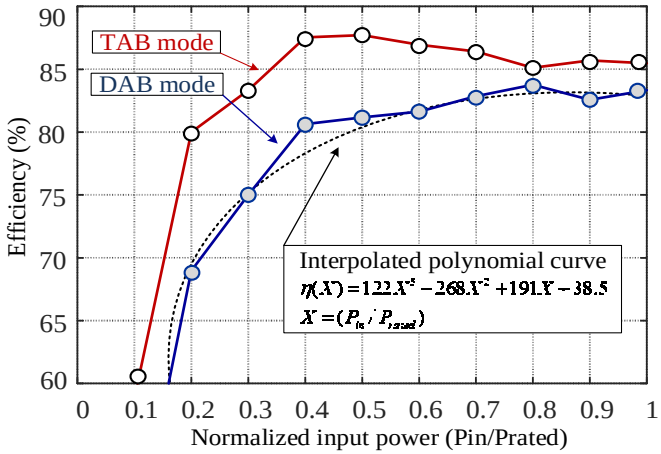

Fig.8- The efficiency characteristics of the converter in the TAB and DAB operation modes and the fitted third-order polynomial.

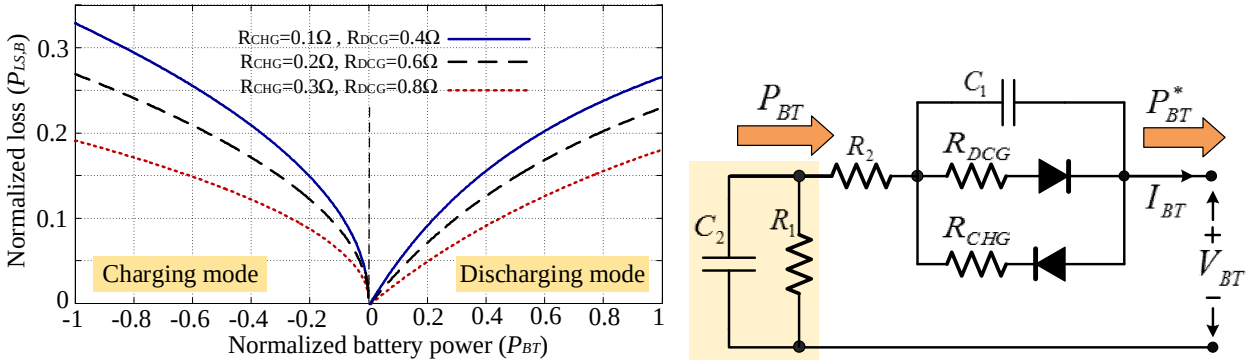

(a) (b)

Fig.9- (a).The battery loss characteristics and (b), the battery equivalent electrical model

account the charging (R_{CHG}) and discharging (R_{DCG}) resistances as presented in Fig.9 (a). The battery efficiency during the charge (η_{BT}^{CHG}) and discharge (η_{BT}^{DCG}) process is defined based on the battery equivalent electrical model presented in Fig.9 (b) from [35]:

$$\eta_{BT}^{CHG} \approx (\eta_{BT}^{DCG})^{-1} = \frac{P_{BT}}{P_{BT}^*} = 1 - \left| \frac{V_{OC} - \sqrt{V_{OC}^2 - 4RP_{BT}^*}}{2V_{OC}} \right| \quad (5)$$

where P_{BT} is the battery cells power, P_{BT}^* the battery terminal power, R the charge or discharge loss resistor and V_{OC} the battery open-circuit voltage. The battery SOC level defined as SOC_{min}, SOC_{med} and SOC_{max} for the minimum, medium and maximum levels respectively is considered as another constraint from

$$\begin{cases} SOC_{med} < SOC < SOC_{\max} & Storage\ \ Application \\ SOC_{\min} < SOC < SOC_{med} & Off-grid\ \ Application \end{cases} \quad (6)$$

On the other hand, the power limit constraints are the maximum power of battery during the charge and the discharge ($P_{BT,max}$), the range of fuel cell power (P_{BFmin} and P_{FCmax}) for operation in the linear characteristics area, the maximum power that can be transferred to/from the grid ($P_{GD,max}$), and the maximum power of electrolyzer ($P_{EL,max}$).

$$\begin{cases} P_{BT} \le P_{BT,\max} & Battery\ \ Power Limit \\ P_{GD} \le P_{GD,\max} & Grid\ Power-transfer Limit \\ P_{EL} \le P_{EL,\max} & Electrolyer\ \ Power Limit \\ P_{FC,\min} < P_{GD,\max} \le P_{FC,\max} & Fuel\ Cell\ Power Limit \end{cases} \quad (7)$$

As can be seen in Fig.7, the procedure starts with applying a positive or negative change (either *δSOC*, *δSOH* or both) to the current value of SOC and SOH levels as the dynamic variables, for a time-step ahead (ΔT_i). A positive or negative value of *δSOC* means a charging or discharging status for the battery respectively and a zero value means a standby mode (no charge or discharge). Similarly, the positive or negative values of *δSOH* mean an active status for electrolyzer or fuel cell respectively and a zero value deactivates both of them for the respected time-step. The amounts of P_{BT}, P_{EL} and P_{FC} then can be calculated accordingly taking into account the constraints in (6)-(7). On the other hand, the forecasted power profiles of the PV generation and load demand are used to estimate the amounts of P_{PV} and P_{LD} for the specified time-step. Finally, the power transferred to/from the grid (P_{GD}), the power loss in the converters and the total power loss (P_{LS}) is determined by using (2)-(4) and the power flow model of the system illustrated in Fig.4.

As the objective function is to minimize the energy bill, the cost of energy received from the grid [C_B^i] and the benefits from sending energy to the grid [C_S^i] for the time-step *i* should be determined from

$$C_S^i = \left[P_{GD}^i * C_{GD\_Sell}^i * \Delta T_i\right], \ if\ P_{GD}(\Delta T_i) \langle 0 \tag{8}$$

$$C_B^i = \left[P_{GD}^i * C_{GD\_Buy}^i * \Delta T_i\right], \ if\ P_{GD}^i(\Delta T_i) \rangle 0 \tag{9}$$

where C_{GD_Buy} and C_{GD_Sell}, are respectively the cost of the energy received from and sold to the grid. The total energy cost for a path considering *n* steps for each time-frame is determined by

$$C^i = \sum_{i=1}^{n} \left[C_S^i + C_B^i\right] \tag{10}$$

Finally, to find the variation path with the minimum energy cost, the resultant cost of all possible paths should be compared. As an example, the two-dimensional searching space based on the SOC and SOH variables and two possible paths presented as R1 and R2 are illustrated in Fig.7.

Different objective functions can be selected according to the system topology, energy generation and demand, energy management scenario. As an example, in the case of a planned off-grid operation or scheduled power outage, the objective function can be adapting the power generation to the load demand during the off-grid operation. Therefore, the path with the minimum difference between the predicted generated power (P_G^i) and the load demand (P_C^i) is selected from

$$C^i = \sum_{i=1}^{n} \left[P_G^i - P_C^i\right] \tag{11}$$

The resulting values of *δSOC*, *δSOH* based on the selected path then are sent to the MSTU to be used in the decision-making process along with the real-time data of the system. The estimated computation time for each evaluation cycle of DP process was less than 10 *ms* which is much less than processing time of real-time control as will be shown in the next section.

3.2. Operation of the real-time rule-based control

The real-time rule-based controller is the main part of the MSTU and is designed to determine the operation mode of the system. The value of *δSOC* and *δSOH* received from the DPU are used to make a decision on the operation of the converter ports. The real-time values of the energy difference between the PV power generation and load demand $\Delta P(n)$, and the difference between energy prices of the grid and fuel cell $\Delta C(n)$ are calculated in real-time data processor as the other input parameters from

$$\Delta C(n) = [C_{GD\_Buy}(n) - C_{FC}(n)], \ \Delta P(n) = [P_{LD}(n) - P_{PV}(n)] \tag{12}$$

They are used to include the energy cost and the power difference in the decision-making process. Fig.10 (a) shows the real-time rule-based control strategy. As can be seen, the process starts with the evaluation of ΔP, which can be positive or negative for PV generation less than or more than the load demand. In the first case, ΔP can be covered by one of the fuel cell, battery or the utility grid depending on the amount of power considering the available hydrogen storage (*δSOH*) and the battery capacity (*δSOC*) received from DPU and the energy cost. In the second case, the surplus energy generated by PV can be supplied to the battery, grid or consumed by electrolyzer considering the available capacity of the battery (*δSOC*) and hydrogen storage (*δSOH*). In the case of supplying energy to the grid, the grid acknowledgment signal (P_{GD_Signal}) is required. The last priority is given to the dump loads such as water heating or electrical heaters. To avoid the fluctuations of the operation modes due to the variation of power difference at the boundary values, hysteresis functions with adjustable hysteresis bands are employed. An example of a comparing block with the applied hysteresis function is illustrated in Fig.10 (b).

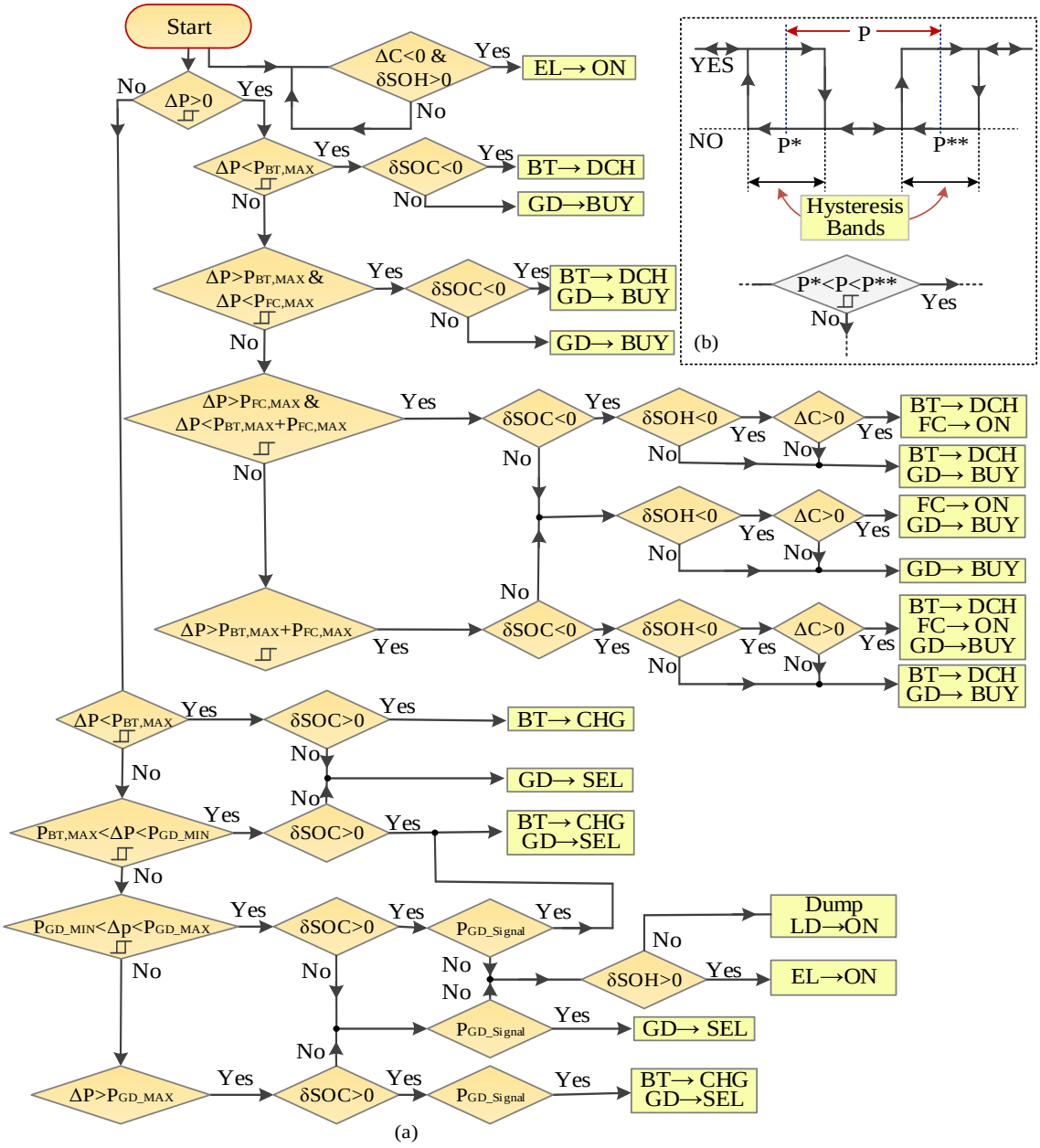

Fig.10-(a) The overall mode selection strategy designed in the MSTU based on the real-time data where DCH stands for discharge, CHG for a charge, SEL for selling power to the grid and, BUY for purchasing power from the grid. (b) a hysteresis-based comparison block.

4. Hardware design and development

A prototype of the proposed system was designed and developed for a residential house with a maximum power of 4.5 kW and the average daily energy consumption of 22 kWh. Fig.11 illustrates the hardware schematic and connection diagram of the designed system including PWM and data transfer pins of the DSPs (TMS320F28335). The designed prototype and the experimental test bench are presented in Fig.12. The system level control, energy management and monitoring are performed by a windows laptop (CPU Intel-core i7, 2.6 GHz, 12 GB RAM) and two digital signal processors (DSPs) are used at the device level to control the dc-dc converters and the inverter. The renewable energy system and the residential loads are connected to the utility grid through a bidirectional meter and a controlled static transfer switch (STS). The STS is controlled by a fault detection and protection unit to disconnect and reconnect the system to the utility grid in case of detecting a faulty grid condition such as over/under voltage or over/under frequency and maintain the anti-islanding operation in blackouts. When the grid fault is cleared, the inverter operation is changed from off-grid to grid-connected mode through a synchronization process. A seamless transition can be realized by proper control of the STS, slowly ramping up the reference signals in the inverter and synchronization to the grid as presented in [36].To drive the IGBT switches, a two channels hybrid integrated driver circuit (VLA567-01R) was selected

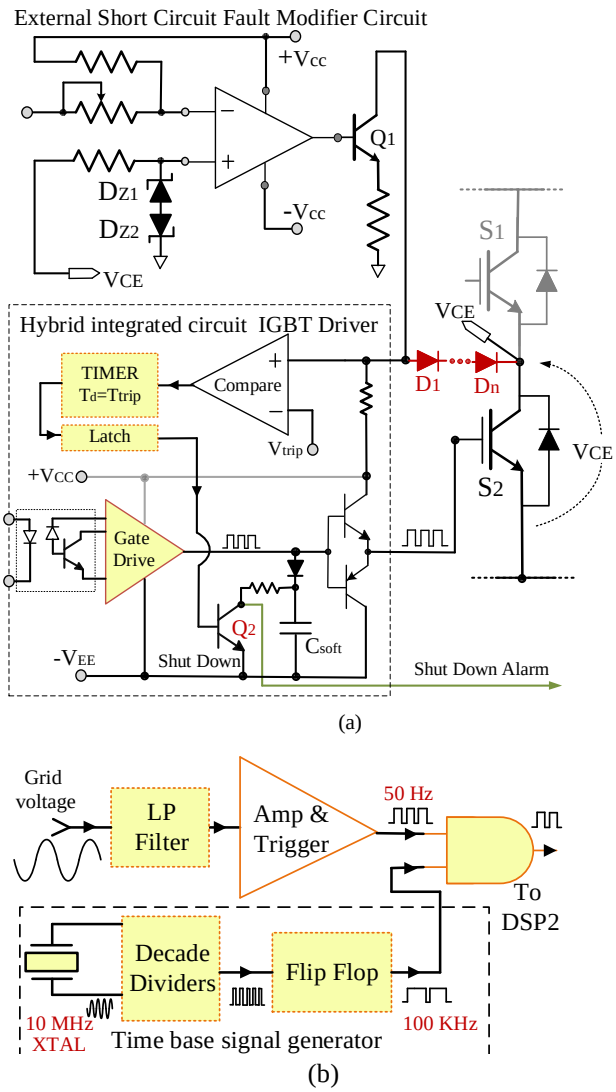

Fig.13- (a) short circuit protection using desaturation detection circuit and modified external comparator and, (b) frequency fault detection

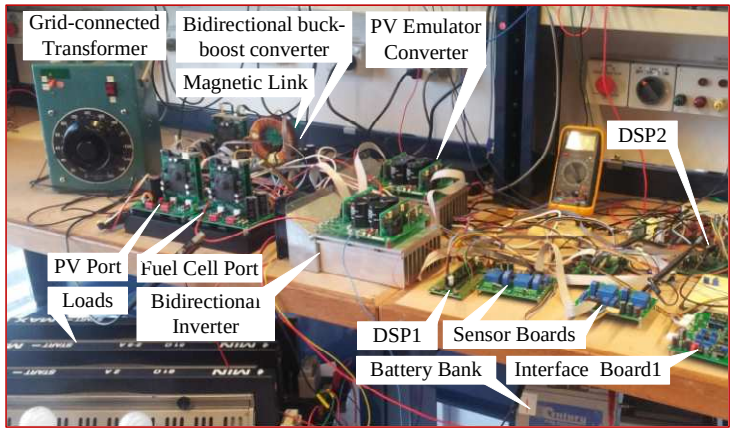

Fig.12-Prototype of the proposed system and the experimental test bench

Table.1 Standards of the Grid-connected Inverters

	Set Point	Trip Delay Time	Maximum
Undervoltage (V<)	180 V	1 S	2 S
Overvoltage 1 (V>)	260 V	1 S	2 S
Overvoltage 2 (V>>)	265 V	—	0.2 S
Under-frequency (f<)	47 Hz	1 S	2 S
Over-frequency (f>)	52 Hz	—	0.2 S

due to its capabilities such as built-in isolated dc-dc converter and short circuit protection, high voltage isolation (2500 V, rms) and high driving current (8 A, peak). As short circuit protection and gate drive circuit are packed together, the gate signal can be immediately shut down in the case of short circuit detection. The short circuit protection operates based on the desaturation detection where the collector-emitter voltage of each switch (V_{CE}) is monitored during the ON state and is compared to a reference trip voltage. In the case of a short circuit, the saturation voltage exceeds the trip voltage and a gate shut down signal is generated as presented in Fig.13 (a). As the internal trip voltage is fixed, to adjust the short circuit trip voltage according to the switch characteristics, diodes D_1 to D_n can be used in a limited range. In this paper, the operation is modified by using an external comparator. The gate shut down signal is activated for a limited time (1-2 *ms*) which is enough for DSP to reduce the gate voltage. A soft gate shut down is achieved by using capacitor C_{soft} to suppress the surge voltages at the shutdown instance. The residential grid-connected inverters mainly operate as a grid-following inverter with the ability to only inject active power to the grid (by controlling current and phase angle). However, using intelligent inverters with the ability to operate as a grid-forming inverter is encouraged and recommended in the recent standard codes (AS/NZS 4777), but still is not operational. The low-voltage, high-voltage and over-current alarms are also generated by comparing the measured values to the references using high-speed window comparators according to the recent standards for grid-connected household RESs presented in Table. 1[15], [16]. On the other hand, under and over frequency alarm signals with a reaction time of less than 50 *ms* and accuracy of 0.1 % (0.05 Hz) are generated by using the circuit presented in Fig.13 (b).

5. Experimental tests

Fig.14 presents two examples of direct and indirect mode transitions that are controlled in MSTU. In the first case, the operation mode changes from M3 where the load is supplied by the grid and fuel cell to M4 where the fuel cell is replaced by the battery due to the load reduction. As can be seen, M12

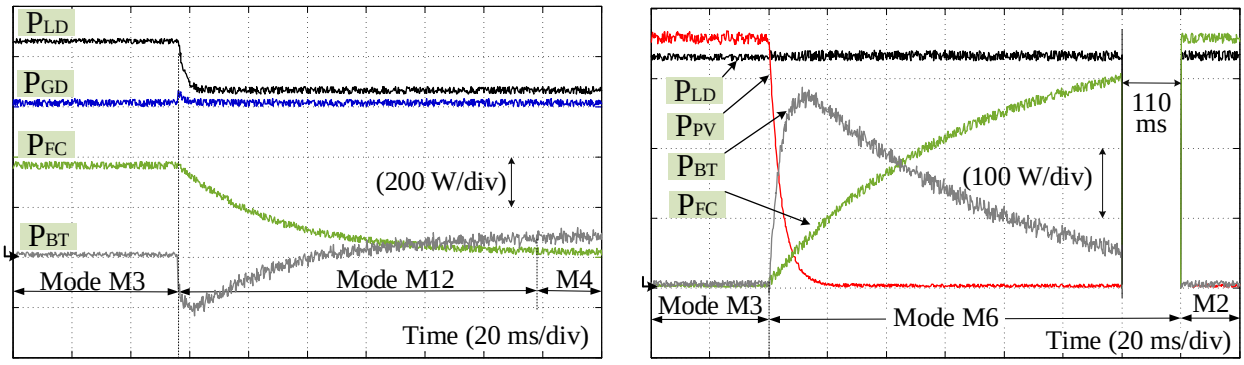

(a) (b)

Fig.14-Operation of MSTU for two cases mode transition, (a) from M3 to M4, where M12 is used as bridging mode, and (b) off-grid condition, from M3 to M2 where M6 is used as bridging mode due to the slow dynamic of the fuel cell.

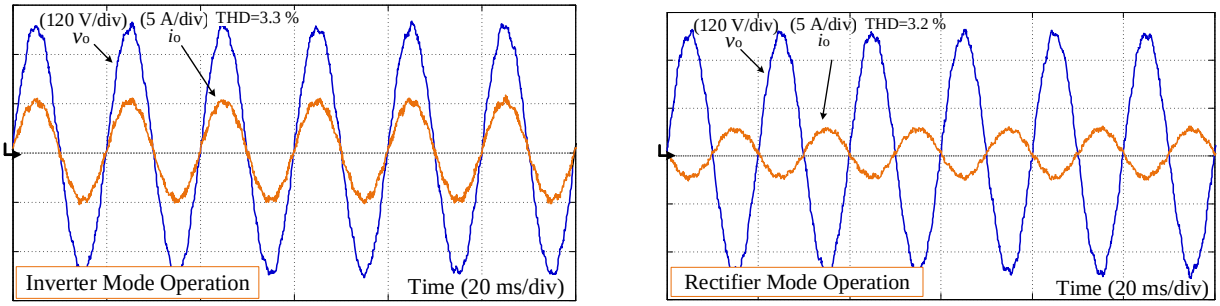

(a) (b)

Fig.15- Experimental waveforms of the inverter output in (a) inverter mode and, (b) rectifier mode

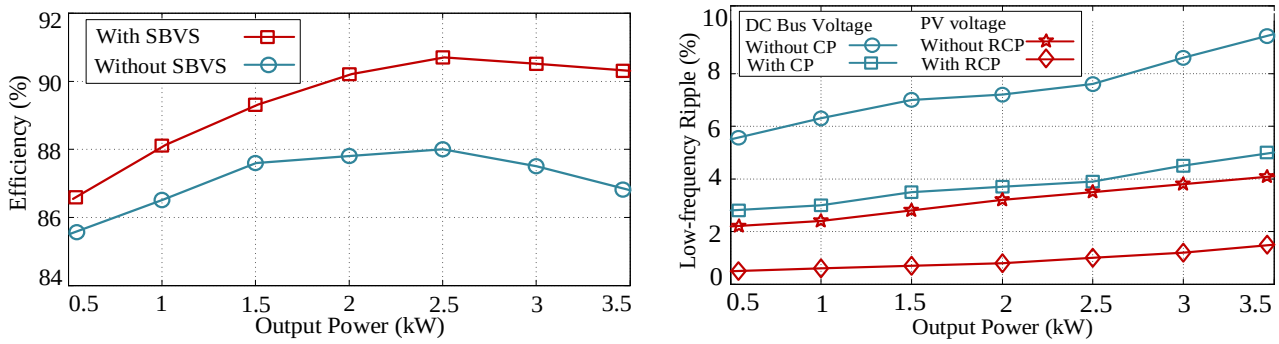

(a) (b)

Fig.16- (a) The effect of using SBVS technique on the efficiency of the proposed HRES, and (b) the effect of using resonant compensation (RCP) in the PV control loop on the PV voltage ripple and compensator (CP) in the inverter control loop on high-voltage dc bus ripple.

is used as the bridging mode due to the slow dynamics of the fuel cell. In the second case, the system is operating in off-grid condition and the mode changes from M3 to M2 where the PV power drops to zero and the fuel cell is going to supply the load. However, M12 is selected as operation mode where the battery is activated in to compensate for the slow dynamics of the fuel cell during transition time which takes about 230 ms in total. Fig.15 illustrates the inverter output voltage and current in both inverter and rectifier modes. As can be seen, the output current is a sinusoidal waveform with total harmonic distortion (THD) less than 5 % according to the standards (IEEE 1547 and IEC 61727). Fig.16 (a) shows that using SBVS technique has increased the efficiency of the system by 4 % when the output power is 3.5 kW. Fig.16 (b) shows that the low-frequency ripple in the PV output voltage is reduced by 3 % as a result of using resonant compensator (RCP) in the PV current control loop. On the other hand, the low-frequency ripple propagated from the inverter output on the high-voltage dc bus is reduced by 4.5 % by using the compensator block (CP) in the inverter control loop. The main advantage of using proposed control techniques is their realization in the software form in the control loop which does not require any extra hardware implementation. In contrast, improvement of efficiency using some of the soft-switching techniques or reducing the ripples using a huge passive component in the low-pass filter need extra hardware design, control complexities and increase the entire system size and cost.

The performance of the proposed EMU is experimentally validated using the test bench shown in Fig.12. Two groups of constant and variable resistors

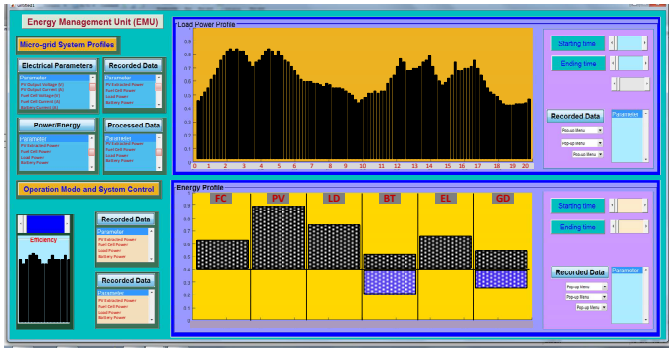

Fig.17- The graphical user interface designed in MATLAB for data record, monitoring and the energy management of the proposed HRES.

are connected in parallel to model a residential load. To model a 24-hours residential load starts from 12 AM, each 2 min duration time is down-scaled to 10s in the test procedure and in total, 720 samples are recorded.

To record and monitor the system parameters a graphical user interface (GUI) is developed using MATLAB as presented in Fig.17. The main recorded data include energy profiles of the PV, fuel cell, battery, load and grid, the history of the system operating modes and faults and input and output data. The PV generation and load demand profiles are scheduled to change according to a typical sunny day profile. It is assumed that the system is in grid-connected condition with a flexible flow to/from the grid. The power limit constraints for the battery, electrolyser, fuel cell and the grid are determined as 500 W, 600 W, 500 W and 1 kW respectively. Fig.18 illustrates the power profiles of the PV (P_{LD}), residential load (P_{LD}), fuel cell (P_{FC}), battery (P_{BT}), and the inverter for the 24-hour test duration. Furthermore, the variation in battery SOC, fuel cell SOH, and the energy cost profiles are presented in details.

The operation modes of the system during the test are presented at the bottom of the battery power profile. The system operation starts with M4 as PV port is off and the battery supplies the power due to the small amount of load demand and lower cost of the battery compared to the grid. On the other hand, the battery fully charged and δSOC is negative due to the long-term predictions which allow the battery to be discharged if is required. When the grid cost changed to less than the battery, it is preferred to supply the load and electrolyser and therefore, M1 is selected. As the PV is activated, M2 is selected, and the system operates on this mode whenever the PV power generation is less than the load demand. The operation mode is changed to M11 when PV power generation is more than the load demand and the surplus energy is used to charge the battery according to the predictive controller commands. The additional energy is sent to the main grid due to the battery power constraints. The operation mode then is changed to M2 when the battery is fully charged (SOC=98 %). In the afternoon, when the PV generation is less than load demand, M6 is selected, and the battery supplies the difference due to the lower cost compared to the grid. When $P_{LD}>P_{BT}+P_{PV}$ then fuel cell is activated, and M5 is selected and similarly for $P_{LD}>P_{PV}+P_{BT}+P_{FC}$ then M12 is preferred as the operation mode. At the last time interval, M1 is selected as grid cost reduced to less than that of the battery and fuel cell.

Fig.19 presents the operation of the proposed system assuming a PV power generation profile with the cloudy weather condition. The load demand profile is considered similar to the previous scenario while PV generation and energy cost profiles are different. The selected operation modes are presented and the mode selection process is performed more or less similar. The main difference is that when PV generation drops to less than load demand due to the shading effect, the difference is supplied by the grid instead of the battery as the battery is preferred to be used more effectively for the peak demand period due to the high cost of the grid energy according to the objective function of the predictive control. The effect of predictive control in the first scenario is to make a delay in the battery charging from the beginning of the period to the midday to use the surplus energy of the PV locally to charge the battery instead of the grid energy. Furthermore, the battery discharge happens at the peak demand period when the grid energy cost is the highest and it is predicted that the fuel cell power is not enough to cover the demand. The total energy supplied or received by each element is determined by using the power supplied or absorbed power and the sampling time T_k (equals 2 min). For example, the generated energy by the fuel cell is defined by

$$E_{FC\_24h} = \sum_{k=1}^{720} P_{FC}(k) T_k \tag{13}$$

The energy distribution analysis of the system for the studied scenarios is illustrated in Fig.20.(a) and (b). As can be seen, in the case of a sunny day profile, the PV generates about 5.6 kWh energy and supplies 3.8 kWh to the load (almost 48 % of the load energy). The rest of the load energy is covered by the fuel cell, grid and the battery as 1.3 kWh, 1.55 kWh, and 1.36 kWh respectively. The battery supplied almost 1.4 kWh and absorbed 0.45 kWh for the presented period. Therefore, the SOC is reduced from 98 % at the beginning of the period to 83 % at the end. The total energy loss in the system resulting from switching and conduction losses and core loss of the transformer equals 0.56 kWh. In the case of the cloudy profile, the PV generation is reduced to 4.55 kWh and supplied about 40 % of the load demand. The difference between the PV generation and the load demand due to the shading effects is covered mainly by the grid. The energy loss in the system decreased slightly due to the increase of the utility grid share in supplying the load demand.

The recorded data by EMU is also used to analyse the system operation economically. Fig.21 illustrates the energy cost analysis of the system for the studied scenarios. The total energy cost of each element is calculated by using the average of the supplied or absorbed energy and the energy price at the

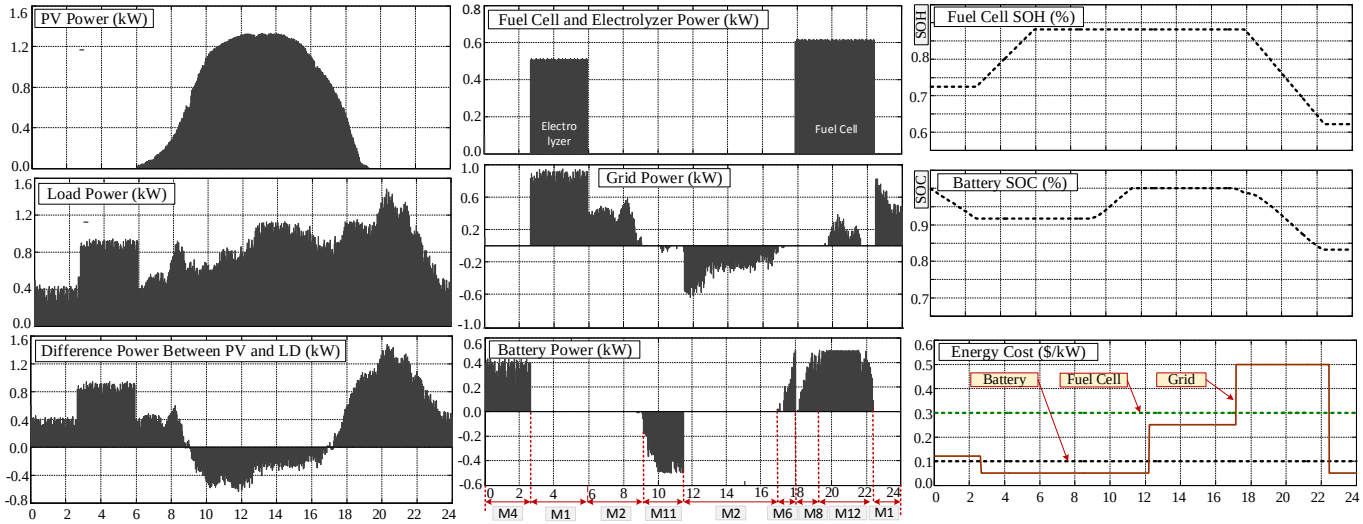

Fig.18- The power profiles of the PV generation (P_{PV}), load demand (P_{LD}), electrolyser (P_{EL}), battery (P_{BT}), fuel cell (P_{FC}) and the grid (P_{GD}) and the battery SOC and fuel cell SOH for the first scenario (a sunny day profile).

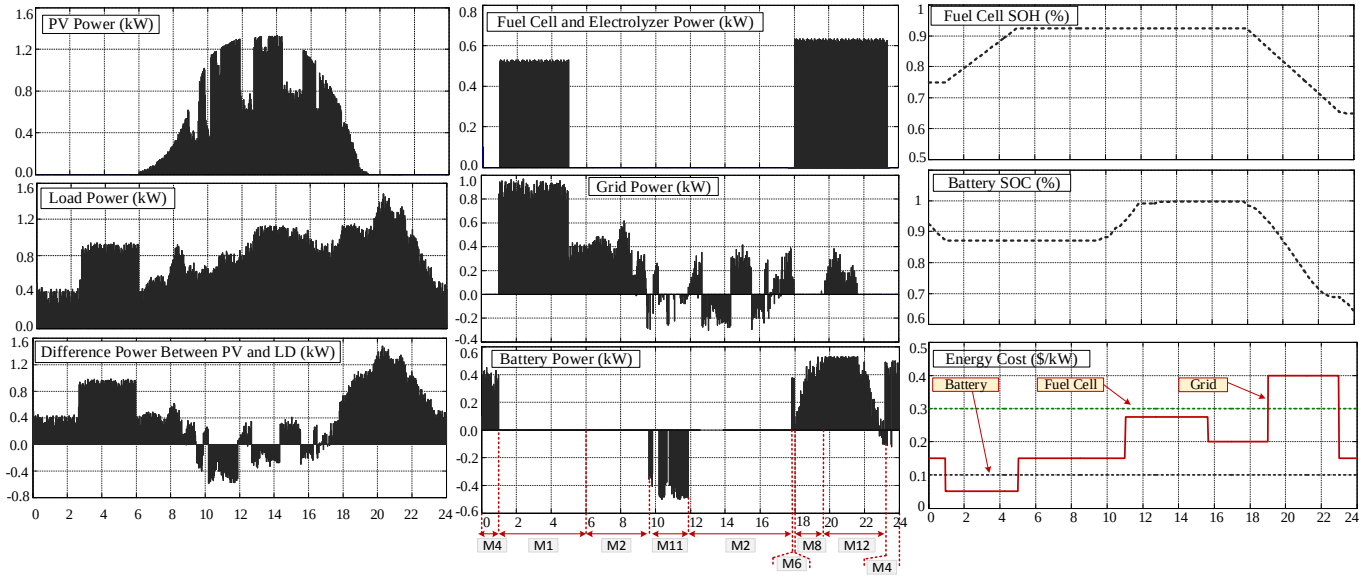

Fig.19-The power profiles of the PV generation (P_{PV}), load demand (P_{LD}), electrolyser (P_{EL}), battery (P_{BT}), fuel cell (P_{FC}) and the grid (P_{GD}) and the battery SOC and fuel cell SOH for second scenario (a cloudy day profile).

sampling times. The total energy cost of the battery (assuming that the battery is preferably charged by either PV or the grid during the off-peak periods), fuel cell and the grid are determined according to the profiles presented in Figs 18 and 19. The energy cost of the renewable energy sources presented in this paper are obtained based on a simple levelized cost of energy (LCOE) using the capital cost of the system and the estimated value of generated energy during the guaranteed life of the system as presented in [37]. For example, considering a 6.5 kW PV system with an estimated generation of 20 kWh/day, about 6500 kWh/year results in 162500 kWh energy after guarantee time (25years). Assuming 6000 $ as the capital installation cost results in about 0.03 $/kWh energy cost. However, there are other effective elements such as operations and maintenance costs, financing and discount issues, degradation and future replacement costs which can effectively change the final result. A more detailed analysis of estimating energy cost for each renewable source can be found in [38]. Similar estimations have been used to estimate the cost of energy for the battery and fuel cell. In the case of grid energy, the average cost of energy in Australia provided by the energy retailers for residential consumers has been taken into account. However, to show the capability of the energy management unit and cover more possible operation modes, more variation steps is applied to the grid energy cost profile.

The analysis shows that customer benefits from selling energy to the grid at peak demand periods in the first and the second scenarios are about 0.38 $/day and 0.11 $/day respectively according to the provided grid energy cost profile. About 56 % (0.38 $/day) and 63 % (0.47 $/day) of the load expenses

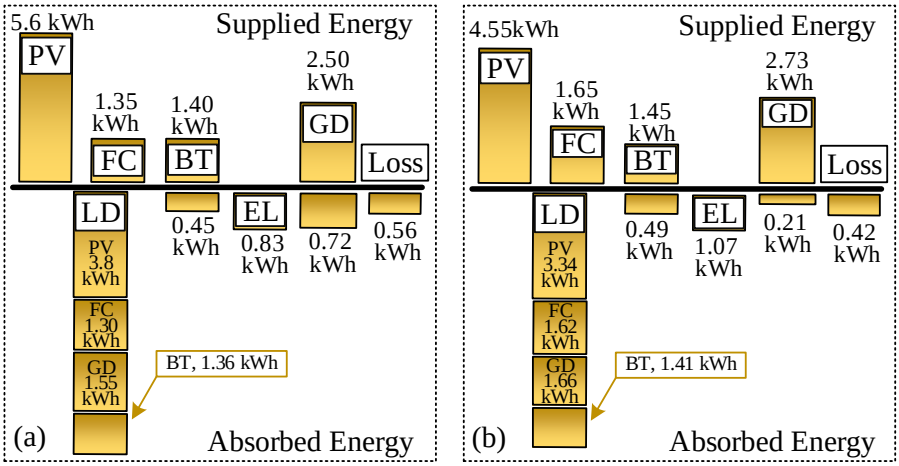

Fig.20- Analysis of the energy distribution of the system for (a) a sunny day and (b) a cloudy day PV generation profiles

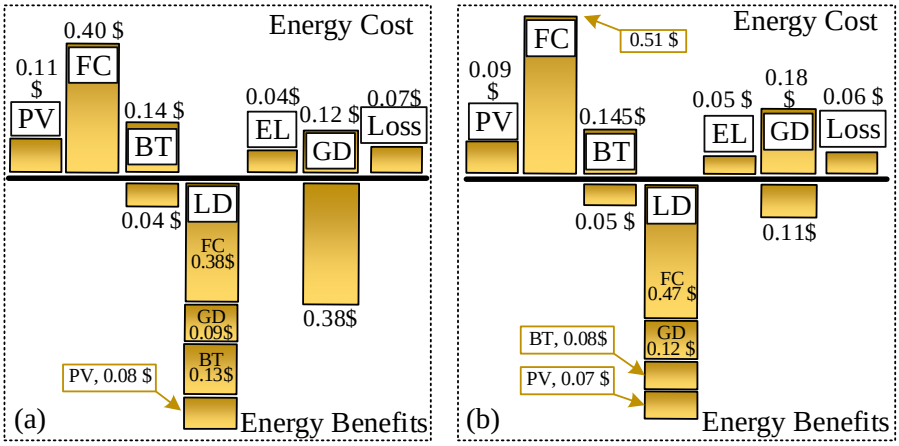

Fig.21- Analysis of the energy cost of the system for (a) a sunny day and (b) a cloudy day PV generation profiles

in the first and the second scenarios are related to the fuel cell. The total energy cost of the system for the studied period is about 0.46 $/day in the first and 0.87 $/day in the second scenario which is much less than the case that the load with the same power profile is only supplied by the grid (about 2.23 $/day) considering the same load demand and energy cost profiles. Therefore, the total energy cost of the consumer is reduced by 80 % for a typical sunny day and 60 % in a cloudy day by using the proposed HRES and energy management technique.

6. Conclusion

A topology of a magnetically coupled hybrid renewable energy system has been presented in this paper. The steady-state operation, energy management method and hardware implementation have been studied. A rule-based real-time controller was combined to a predictive dynamic programming based optimization technique to optimally manage the energy distribution in the micro-grid according To adapt the system features according to the current standards of grid-connected residential systems, different control techniques and hardware designs are employed. The proposed energy management and the control techniques are validated through experimental tests using a developed prototype. It was shown that the efficiency performance of the system increased by 4 % by using the SBVS technique. The feed forward compensator reduced the low-frequency ripples reflected on the HVDC bus by 4 % and the current ripple of the PV port reduced by 5 % as a result of using the resonant compensator. It was shown that the total energy cost is reduced from 2.13 $/day in the case of using utility grid only to 0.315 $/day (based on the assumed energy cost profiles) by using proposed renewable energy system.

REFERENCES

[1] Nikos Hatziargyriou, “The Microgrids Concept,” *Microgrids: Architectures and Control* , 1, Wiley-IEEE Press, 2014

[2] J. Rocabert, A. Luna, F. Blaabjerg and P. Rodríguez, “Control of Power Converters in AC Microgrids,” *IEEE Trans. Power Elec.* vol. 27, no. 11, pp. 4734-4749, Nov. 2012.

[3] R. Majumder, “Some Aspects of Stability in Microgrids,” *IEEE Trans. Power Systems*, vol. 28, no. 3, pp. 3243-3252, Aug. 2013.

[4] Australian Renewable Energy Agency Annual report 2016/2017 at: https://arena.gov.au/assets/2017/10/2016-2017-arena-annual-report.pdf

[5] Clean Energy Australia Report 2016 at: http://gccn.org.au/wp-content/uploads/2017/12/Clean-Energy-Australia-Report-2016.pdf

[6] Digambar M. Tagare, "Hybrid Systems," *Electricity Power Generation: The Changing Dimensions*, 1, Wiley-IEEE Press, 2011, pp.352

[7] P. Li, R. Dargaville, F. Liu, J. Xia and Y. D. Song, "Data-Based Statistical Property Analyzing and Storage Sizing for Hybrid Renewable Energy Systems," *IEEE Trans.Ind.Electron.*, vol. 62, no. 11, pp. 6996-7008, Nov. 2015.

[8] Tao, H.(2008).Phd thesis, "Integration of sustainable energy sources through power electronic converters in small distributed electricity generation systems" Eindhoven: Technische Universiteit Eindhoven .

[9] H. Tao, A. Kotsopoulos, J. L. Duarte, and M. A. M. Hendrix, "Family of multiport bidirectional DC–DC converters," *IEE proceedings of Electric Power Applications*, Vol.153, Issue: 3, pp.451-458, 2006

[10] H. Wu, P. Xu, H. Hu, Z. Zhou and Y. Xing, "Multiport Converters Based on Integration of Full-Bridge and Bidirectional DC–DC Topologies for Renewable Generation Systems," *IEEE Trans. Ind. Electron.*, vol. 61, no. 2, pp. 856-869, Feb. 2014.

[11] C. Zhao, S.D.Round, and J.W.Kolar, "An isolated three-port bidirectional DC–DC converter with decoupled power flow management," *IEEE Trans. Power Electron.*, vol. 23, no. 5, pp. 2443–2453, Sep. 2008.

[12] Y. C. Liu and Y. M. Chen, "A Systematic Approach to Synthesizing Multi-Input DC–DC Converters," *IEEE Trans. Power Electron.*, vol. 24, no. 1, pp. 116-127, Jan. 2009.

[13] N. D. Benavides and P. L. Chapman, "Power budgeting of a multiple-input buck-boost converter," *IEEE Trans. Power Electron.*, vol. 20, no. 6, pp. 1303-1309, Nov. 2005.

[14] M. Jafari, Z. Malekjamshidi, G. Lei, T. Wang, G. Platt and J. Zhu,"Design and Implementation of an Amorphous High-Frequency Transformer Coupling Multiple Converters in a Smart Microgrid,"*IEEE Trans. Ind. Electron.*, vol. 64, no. 2, pp. 1028-1037, Feb. 2017.

[15] https://shop.standards.govt.nz/catalog/4777.2:2015 (AS%7CNZS)/scope

[16] https://webstore.iec.ch/preview/info_iec62109-1%7Bed1.0%7 Den.pdf

[17] https://standards.ieee.org/findstds/standard/1547-2018.html

[18] Hu.M, Xiao.J.W, Cui.S.C, Wang.Y.W, "Distributed real-time demand response for energy management scheduling in smart grid," *International Journal of Electrical Power & Energy Systems*, Vol.99,pp. 233-245, 2018.

[19] Bahl.B, Lampe.M, Voll.P, Bardow.A, "Optimization-based identification and quantification of demand-side management potential for distributed energy supply systems" *Energy*,Vol.135, pp 889-899,2017.

[20] Y. Riffonneau, S. Bacha, F. Barruel and S. Ploix, "Optimal Power Flow Management for Grid Connected PV Systems With Batteries," *IEEE Trans. Sustainable Energy*, vol. 2, no. 3, pp. 309-320, July 2011.

[21] L. Zhang and Y. Li, "Optimal Energy Management of Wind-Battery Hybrid Power System With Two-Scale Dynamic Programming," *IEEE Trans.Sustainable Energy*, vol. 4, no. 3, pp. 765-773, July 2013.

[22] H. Kanchev, D. Lu, F. Colas, V. Lazarov and B. Francois, "Energy Management and Operational Planning of a Microgrid With a PV-Based Active Generator for Smart Grid Applications," *IEEE Trans. Ind.Electron.*, vol. 58, no. 10, pp. 4583-4592, Oct. 2011.

[23] C. Wang and M. H. Nehrir, "Power Management of a Stand-Alone Wind/Photovoltaic/Fuel Cell Energy System," *IEEE Trans. Energy Conversion*, vol. 23, no. 3, pp. 957-967, Sept. 2008.

[24] D. Arcos-Aviles, J. Pascual, L. Marroyo, P. Sanchis and F. Guinjoan, "Fuzzy Logic-Based Energy Management System Design for Residential Grid-Connected Microgrids," *IEEE Trans.Smart Grid*, vol. 9, no. 2, pp. 530-543, March 2018.

[25] M. Jafari, Z. Malekjamshidi, D. D. C. Lu and J. Zhu, "Development of a Fuzzy-Logic-Based Energy Management System for a Multi-Port Multi-Operation Mode Residential Smart Micro-grid," *IEEE Trans. Power Elec.* doi: 10.1109/TPEL.2018.2850852

[26] I. Ben Ali, M. Turki, J. Belhadj, X. Roboam, "Optimized fuzzy rule-based energy management for a battery-less PV/wind-BWRO desalination system" *Energy*, Vol.159, pp.216-228, 2018.

[27] M. Koot, J. T. B. A. Kessels, B. de Jager, W. P. M. H. Heemels, P. P. J. van den Bosch and M. Steinbuch, "Energy management strategies for vehicular electric power systems," *IEEE Trans. on Vehicular Tech.* vol. 54, no. 3, pp. 771-782, May 2005.

[28] M.Jafari, Z.Malekjamshidi, J.Zhu, "A magnetically coupled multi-port, multi-operation-mode micro-grid with a predictive dynamic programming-based energy management for residential applications" *International Journal of Electrical Power & Energy Systems*, Vol.104, pp. 784-796.

[29] Y. Shi, R. Li, Y. Xue and H. Li, "High-Frequency-Link-Based Grid-Tied PV System With Small DC-Link Capacitor and Low-Frequency Ripple-Free Maximum Power Point Tracking," *IEEE Trans. Power Electron.*, vol. 31, no. 1,pp. 328-339, Jan. 2016.

[30] F. Liu, S. Duan, F. Liu, B. Liu and Y. Kang, "A Variable Step Size INC MPPT Method for PV Systems," *IEEE Trans. Ind. Electron.*, vol. 55, no. 7, pp. 2622-2628, July 2008.

[31] G. R. Chandra Mouli; J. Schijffelen; P. Bauer; M. Zeman, "Design and Comparison of a 10kW Interleaved Boost Converter for PV Application Using

Si and SiC Devices," *IEEE Journal of Emerging and Selected Topics in Power Electronics* , vol. PP, no.99, pp.1-1,2016.

[32] B. Yang, W. Li, Y. Zhao and X. He, "Design and Analysis of a Grid-Connected Photovoltaic Power System," *IEEE Trans. Power Electron.*, vol. 25, no. 4, pp. 992-1000, April 2010.

[33] M. P. Kazmierkowski and L. Malesani, "Current control techniques for three-phase Voltage-Source PWM Converters: A survey," *IEEE Trans. Ind. Electron.*, vol. 45, no. 5, pp. 691–703, Oct. 1998.

[34] A. Karimi, D. Garcia and R. Longchamp, "PID controller tuning using Bode's integrals," *IEEE Trans. Control Systems Technology*, vol. 11, no. 6, pp. 812-821, Nov. 2003.

[35] P. Fortenbacher, J. L. Mathieu and G. Andersson, "Modeling and Optimal Operation of Distributed Battery Storage in Low Voltage Grids," *IEEE Trans.on Power Systems*, vol. 32, no. 6, pp. 4340-4350, Nov. 2017.

[36] Tirumala R, Mohan N, Henze C. Seamless transfer of grid-connected PWM inverters between utility-interactive and stand-alone modes. In: APEC. Seventeenth annual IEEE applied power electronics conference and exposition (Cat. No.02CH37335), Dallas, TX, USA, vol. 2; 2002. p. 1081 – 6.

[37] https://www.solarpowerworldonline.com/2016/05/calculate-solar-lcoe-understand-values/

[38] Ioannis Koumparou, Georgios C. Christoforidis, Venizelos Efthymiou, Grigoris K. Papagiannis, George E. Georghiou, Configuring residential PV net-metering policies – A focus on the Mediterranean region, Renewable Energy, Volume 113, 2017, Pages 795-812.